Supporting Information

# Self-assembled sandwich-like MXene-derived nanocomposites for enhanced electromagnetic wave absorption

**Guoliang Zhao [a, 1], Huipeng Lv [b, 1], Yang Zhou [a], Xiaotong Zheng [c], Chen Wu [b, *], Chen Xu [a, *]**

[a] *Institute of Materials, China Academy of Engineering Physics, Jiangyou City 621908, Sichuan, China*

[b] *School of Materials Science and Engineering, State Key Laboratory of Silicon Materials, Key Laboratory of Novel Materials for Information Technology of Zhejiang Province, Zhejiang University, Hangzhou 310027, China*

[c] *School of Materials Science and Engineering, Southwest Jiaotong University, Chengdu 610031, China*

[1] These two authors contributed equally to this work

*Corresponding authors: chenxuacademic@163.com; chen_wu@zju.edu.cn.

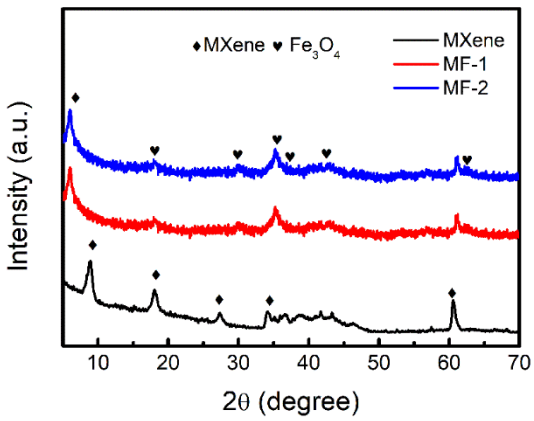


Figure S1 XRD patterns of the pristine MXene, MF-1 and MF-2.

Figure S1 shows the XRD patterns of the pristine MXene, MF-1 and MF-2. Additional peaks corresponding to the $Fe_3O_4$ phase are observed for both sample MF-1 and MF-2 compared with the pristine MXene, indicating the formation of the $Fe_3O_4$ during the hydrothermal process.

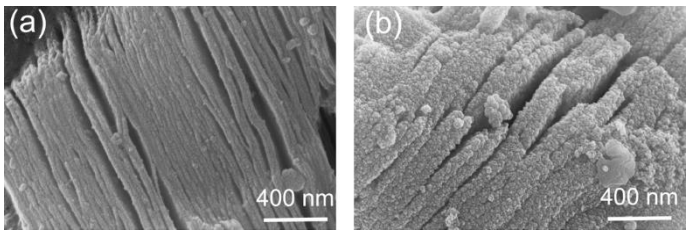


Figure S2. SEM images of sample (a) MF-1 and (b) MF-2.

Figure S2 shows the morphology of the MF-1 and MF-2. Only a few spherical nanoparticles are formed for sample MF-1 (Figure S2a), and the nanoflakes of $Ti_3C_2T_x$ stack together to form relative thicker flakes. With increased amount of $FeCl_3 \cdot 6H_2O$ in the precursor, the $Ti_3C_2T_x$ MXene is covered homogenously with raised content of nanoparticles with maintained layer structure.

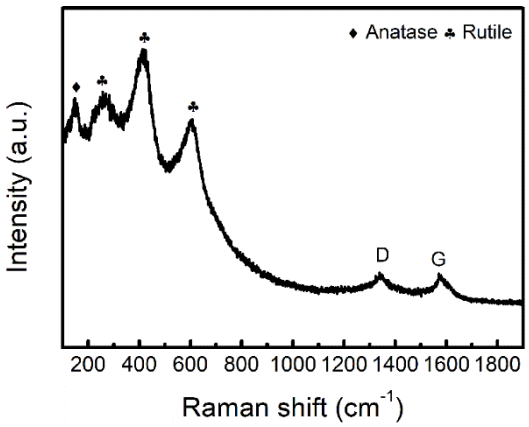


Figure S3. Raman spectrum of sample MF-3.

Figure S3 shows the Raman spectrum of the MF-3, the peak at 144 $cm^{-1}$ confirms the formation of anatase $TiO_2$ during the hydrothermal process. The peaks at 271 $cm^{-1}$, 418 $cm^{-1}$, and 606 $cm^{-1}$ also suggest the formation of rutile $TiO_2$[2-3]. The peaks at 1340 $cm^{-1}$ and 1570 $cm^{-1}$ can be assigned to D and G bands of graphitic carbon[4].

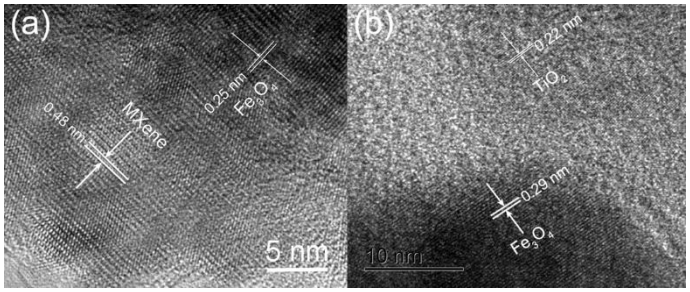


Figure S4. (a), (b) HRTEM images of MF-3.

Figure S4 shows the HRTEM images of MF-3, the lattice spacing of 0.25 nm and

0.29 nm can be assigned to the (311) and (220) planes of the $Fe_3O_4$. The lattice spacing of 0.48 nm corresponds to typical (0004) plane of the hexagonal structure of MXene, and the lattice spacing of 0.22 nm can be attributed to the (111) plane of the rutile $TiO_2$.

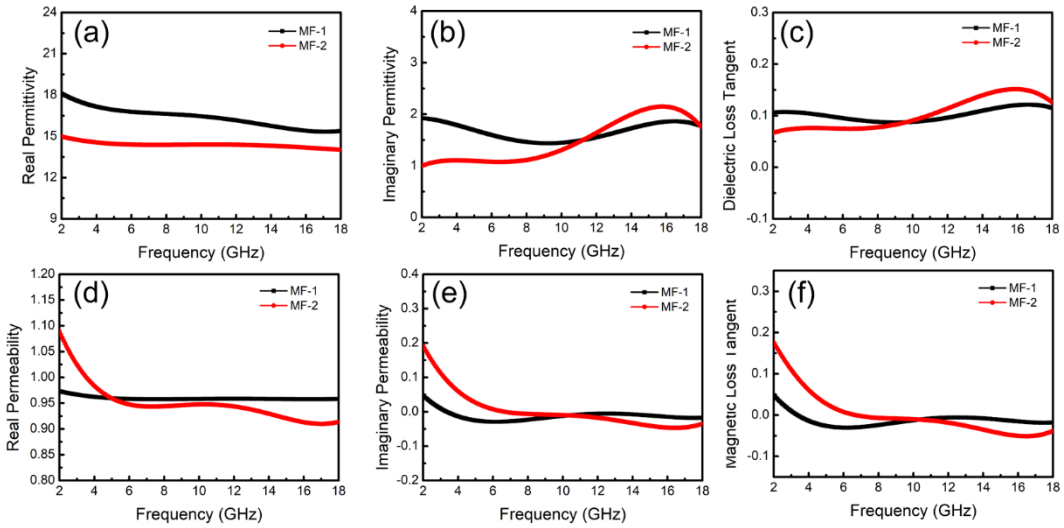


Figure S5. Electromagnetic parameters and loss tangent of the MF-1 and MF-2, including the (a) real part (ε′) and (b) imaginary part ($\varepsilon''$) of permittivity, (c) dielectric loss tangent ($\tan\delta_e = \varepsilon''/\varepsilon'$), (d) real part (μ′) and (e) imaginary part ($\mu''$) of permeability and (f) magnetic loss tangent ($\tan\delta_m = \mu''/\mu'$).

Figure S5 shows the permittivity and permeability of the MF-1 and MF-2. After the introduction of $Fe_3O_4$ nanoparticles, both $\varepsilon'$ and $\varepsilon''$ of the MXene/$Fe_3O_4$ samples become much smaller than those of the pristine MXene. With increased amount of $Fe_3O_4$, the $\varepsilon'$ of the MF samples decreases (Figure S5a and Figure 4a). In the lower frequency range from 2 to 10 GHz, both $\varepsilon''$ and $\tan\delta_e$ of the MXene/$Fe_3O_4$ nanocomposites show a decreasing trend with increased $Fe_3O_4$/MXene ratio (Figure S5b-c), while increasing trend of the $\varepsilon''$ and $\tan\delta_e$ are observed with raised $Fe_3O_4$/MXene ratio in the higher frequency range from 10 to 18 GHz (Figure S5b-c).

The $\mu'$, $\mu''$ and $\tan\delta_m$ of the MXene/$Fe_3O_4$ samples all show abrupt rise compared to those of the pristine MXene due to the introduction of the ferromagnetic $Fe_3O_4$ phase, and the $\tan\delta_m$ increases slightly as the $Fe_3O_4$ ratio increases (Figure S5d-f).

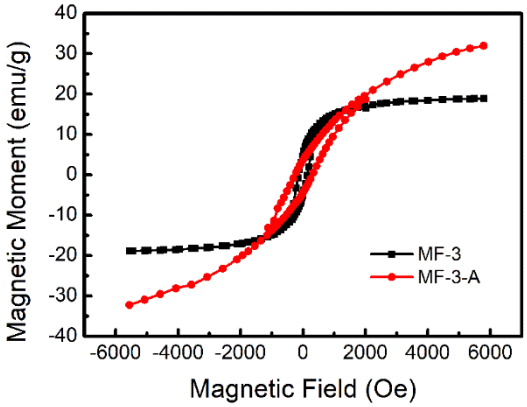


Figure S6. Hysteresis loops taken from the MF-3 and MF-3-A.

Figure S6 shows the hysteresis loops of both sample MF-3 and MF-3-A. Both sample MF-3 and MF-3-A show excellent soft magnetic properties with small coercive force and residual magnetization. Sample MF-3-A possesses higher magnetic moment than that of the MF-3 resulted from the transformation of $Fe_3O_4$ to α-Fe with enhanced magnetization.

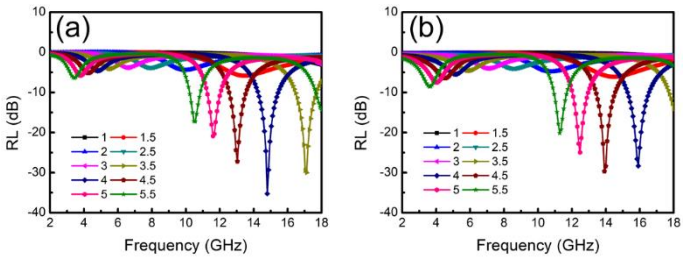


Figure S7. Reflection loss as a function of frequency for the (a) MF-1 and (b) MF-2 with different absorber thickness.

The calculated reflection loss of both sample MF-1 and MF-2 are shown in Figure S7. The minimum RL of MF-1 is -35.2 dB at 14.8 GHz with the thickness of 4 mm, and the minimum RL of MF-2 is -29.7 dB at 13.9 GHz with the thickness of 4.5 mm. Dual peaks are observed in the RL curves in Figure S7 due to multiple possible coefficient which may satisfy the quarter-wavelength thickness relation[5].

We prepared additional sample using the same synthesis method of the $Fe_3O_4$/MXene without the addition of $Fe_3O_4$ (denoted as AM) and have measured the electromagnetic parameters to prove the effect of $Fe_3O_4$. The $\varepsilon'$, $\varepsilon''$ and $\tan\delta_e$ of sample AM increase after the hydrothermal process but the $\varepsilon'$, $\varepsilon''$ and $\tan\delta_e$ of sample MF-3 as its counterpart decrease, which should be mainly caused by the introduction of the $Fe_3O_4$ with large electrical resistivity (Figure S8). For the increased permittivity of MXene treated hydrothermally, on one hand, the amount of $TiO_2$ formed during the hydrothermal process is considerably low that could not be detected by XRD. On the other hand, the newly formed $TiO_2$ introduces more interfaces and correspondingly enhances interfacial polarization which accounts for higher permittivity.

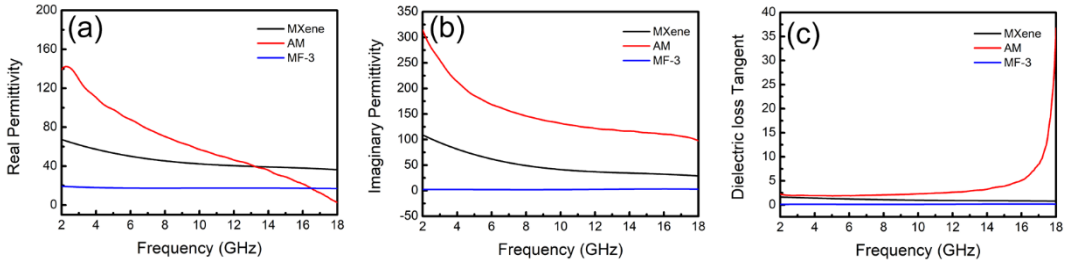


Figure S8. Electromagnetic parameters and loss tangent of the pristine MXene, AM and MF-3, including the (a) real part ($\varepsilon'$) and (b) imaginary part ($\varepsilon''$) of permittivity, (c) dielectric loss tangent ($\tan\delta_e = \varepsilon''/\varepsilon'$).

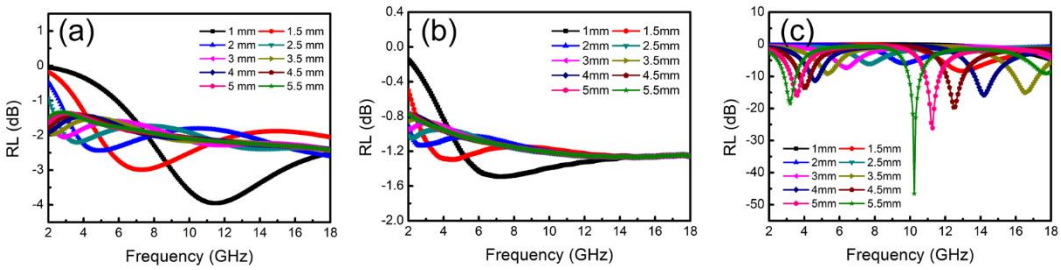


Figure S9. Reflection loss as a function of frequency for the (a) pristine MXene, (b) AM and (c) MF-3 with different absorber thickness.

The RL curves of samples at given frequency and thickness are shown in Figure S9. The pristine MXene shows the minimum RL of only -4 dB at 11.5 GHz. The minimum RL of the AM is -1.5 dB at 7.1 GB, which is even worse than that of pristine MXene. The minimum RL of sample MF-3 has been improved to -46.7 dB at 10.2 GHz with the absorber thickness of 5.5 mm. Thus the improvement of electromagnetic wave absorption properties of sample MF-3 should be mainly caused by the introduction of the $Fe_3O_4$.

Table S1. Electromagnetic wave absorption properties of 2D absorbing materials reported in recent years

| Filler | Matrix | $RL_{min}$ (dB) | Optimum thickness (mm) | The effective bandwidth (GHz) | Refs |
|---|---|---|---|---|---|
| $C/TiO_2/\alpha$-Fe | wax | -45.1 | 1.5 | 3.5 | This work |
| $C/TiO_2$ | wax | −36 | 1.7 | 5.6 | 6 |
| $MXene/TiO_2$ | wax | -48.1 | 1.85 | 2.8 | 7 |
| $Ti_3C_2T_x$ | wax | -30 | 1.8 | 2.8 | 7 |
| ZnO-MXene | wax | -26.3 | 4.0 | 1.4 | 8 |
| $Ti_3C_2T_x$/CNTs | wax | -52.9 | 1.55 | 4.46 | 9 |
| $Co_2Z/Ti_3C_2$ | PVB | -46.3 | 2.8 | 1.6 | 10 |
| $Ti_2CT_x$ | wax | -54.1 | 4.5 | 1.1 | 9 |
| $RGO/Fe_3O_4$ | wax | -40 | 4.5 | ~3 | 11 |
| RGO/ZnO | wax | -25.9 | 3 | 4.68 | 12 |
| $RGO/MnFe_2O_4$ | PVDF | -29 | 3 | 4.8 | 13 |
| RGO/Co | wax | -47.5 | 2 | ~5 | 14 |
| G/Fe | wax | -31.5 | 2.5 | 4.7 | 11 |
| ZnO/RGO | PDMS | -27.8 | 4.8 | 4.2 | 12 |

**Reference**

1. Zhang X. F.; Liu Y.; Dong S.; Ye Z. Y.; Gup Y. One-Step Hydrothermal Synthesis of a $TiO_2$-$Ti_3C_2T_x$ Nanocomposite with Small Sized $TiO_2$ Nanoparticles. *Ceram. Int.* **2017**, *14*, 11065-11070.

2. Li, Z.; Wang, L.; Sun, D.; Zhang, Y.; Liu, B.; Hu, Q.; Zhou, A. Synthesis and Thermal Stability of Two-Dimensional Carbide Mxene $Ti_3C_2$. *Mater. Sci. Eng., B* **2015**, *191*, 33−40.

3. Naguib, M.; Mashtalir, O.; Lukatskaya, M. R.; Dyatkin, B.; Zhang, C.; Presser, V.; Gogotsi, Y.; Barsoum, M. W. One-Step Synthesis of Nanocrystalline Transition Metal Oxides on Thin Sheets of Disordered Graphitic Carbon by Oxidation of Mxenes. *Chem. Commun.* **2014**, *50*, 7420−7423.

4. Ferrari, A. C.; Robertson, J. Interpretation of Raman Spectra of Disordered and Amorphous Carbon. *Phys. Rev. B*. **2000**, *61(20)*, 14095-14107.

5. Wang, B.; Wei, J.; Qiao, L.; Wang, T.; Li F. Influence of the Interface Reflections on the Microwave Reflection Loss for Carbonyl Iron/Paraffin Composite Backed by a Perfect Conduction Plate. J. Magn. Magn. Mater. **2012**, *324 (5)*, 761-765.

6. Han, M. K.; Yin, X. W.; Li, X. L.; Anasori, B.; Zhang, L. T.; Cheng, L. F.; Gogotsi, Y. Laminated and Two-Dimensional Carbon-Supported Microwave Absorbers Derived from MXenes. *ACS Appl. Mater. Inter.* **2017,** *9*, 20038-20045.

7. Han, M. K.; Yin, X. W.; Wu, H.; Hou, Z. X.; Song, C. Q.; Li, X. L.; Zhang, L. T.; Cheng, L. F. $Ti_3C_2$ MXenes with Modified Surface for High-Performance Electromagnetic Absorption and Shielding in the X-Band. *ACS Appl. Mater. Inter.* **2016,** *8*, 21011-21019.

8. Qian, Y.; Wei, H.; Dong, J.; Du, Y.; Fang, X.; Zheng, W.; Sun, Y.; Jiang, Z. Fabrication of Urchin-like ZnO-MXene Nanocomposites for High-Performance Electromagnetic Absorption. *Ceram. Int.* **2017,** *43*, 10757-10762.

9. Li, X.; Yin, X.; Han, M.; Song, C.; Xu, H.; Hou, Z.; Zhang, L.; Cheng, L. $Ti_3C_2$ MXenes Modified with in Situ Grown Carbon Nanotubes for Enhanced Electromagnetic Wave Absorption Properties. *J. Mater. Chem. C.* **2017,** *5*, 4068-4074.

10. Yang, H.; Dai, J.; Liu, X.; Lin, Y.; Wang, J.; Wang, L.; Wang, F. Layered PVB/$Ba_3Co_2Fe_{24}O_{41}$/$Ti_3C_2$ Mxene Composite: Enhanced Electromagnetic Wave Absorption Properties with High Impedance Match in a Wide Frequency Range. *Mater. Chem. Phys.* **2017,** *200*, 179-186.

11. Zheng, X.; Feng, J.; Zong, Y.; Miao, H.; Hu, X.; Bai, J.; Li, X. Hydrophobic Graphene Nanosheets Decorated by Monodispersed Superparamagnetic $Fe_3O_4$ Nanocrystals as Synergistic Electromagnetic Wave Absorbers. *J. Mater. Chem. C.* **2015**, *3*, 4452-4463.

12. Wu F.; Xia Y.; Wang Y.; Wang M. Two-Step Reduction of Self-Assembled Three-Dimensional (3D) Reduced Graphene Oxide (RGO)/Zinc Oxide (ZnO) Nanocomposites for Electromagnetic Absorption. *J. Mater. Chem. C* **2014**, *2*, 20307–20315.

13. Zhang, X. J.; Wang, G. S.; Cao, W. Q.; Wei, Y. Z.; Liang, J. F.; Guo, L.; Cao, M. S. Enhanced Microwave Absorption Property of Reduced Graphene Oxide (RGO)-$MnFe_2O_4$ Nanocomposites and Polyvinylidene Fluoride. *ACS Appl. Mater. Inter.* **2014**, *6*, 7471-7478.

14. Pan, G.; Zhu, J.; Ma, S.; Sun, G.; Yang, X. Enhancing the Electromagnetic Performance of Co through the Phase-Controlled Synthesis of Hexagonal and Cubic Co Nanocrystals Grown on Graphene. *ACS Appl. Mater. Inter.* **2013**, *5*, 12716-12724.

15. Chen, Y.; Lei, Z.; Wu, H.; Zhu, C.; Gao, P.; Ouyang, Q.; Qi, L. H.; Qin, W. Electromagnetic Absorption Properties of Graphene/Fe Nanocomposites. *Mater. Res. Bull.* **2013**, *48*, 3362-3366.

16. Song, C.; Yin, X.; Han, M.; Li, X.; Hou, Z.; Zhang, L.; Cheng, L. Three-Dimensional Reduced Graphene Oxide Foam Modified with ZnO Nanowires for Enhanced Microwave Absorption Properties. *Carbon* **2017,** *116*, 50-58.